Available online at www.sciencedirect.com
ScienceDirect
Journal of Catalysis 253 (2008) 119–131
JOURNAL OF CATALYSIS
www.elsevier.com/locate/jcat

SBA-15-supported nickel phosphide hydrotreating catalysts

Tamás I. Korányi [a,*], Zdeněk Vít [b], Dilip G. Poduval [c], Ryong Ryoo [d], Hei Seung Kim [d], Emiel J.M. Hensen [c]

[a] *Department of Molecular Spectroscopy, Institute of Structural Chemistry, Chemical Research Center of the Hungarian Academy of Sciences, P.O. Box 17, H-1525 Budapest, Hungary*
[b] *Institute of Chemical Process Fundamentals, Academy of Sciences of the Czech Republic, Rozvojová 135, 165 02 Prague 6, Czech Republic*
[c] *Schuit Institute of Catalysis, Eindhoven University of Technology, P.O. Box 513, 5600 MB Eindhoven, The Netherlands*
[d] *National Creative Research Initiative Center for Functional Nanomaterials, Department of Chemistry, KAIST, Daejeon, 305-701, Republic of Korea*

Received 21 August 2007; revised 17 October 2007; accepted 17 October 2007

Available online 26 November 2007

Abstract

A series of Ni_2P and $Ni_{12}P_5$ hydrotreating catalysts supported on SBA-15 ordered mesoporous silica were prepared by impregnation of nickel phosphate precursors followed by reduction in hydrogen at 873 K. The major product was Ni_2P with additional phosphate species when a high excess of phosphorus was used (P/Ni = 2). When a stoichiometric amount of P was used (P/Ni = 0.5), the sole product was $Ni_{12}P_5$ without Ni_2P and phosphate byproducts. The active site density as determined by CO chemisorption for such $Ni_{12}P_5$ phases was about three times higher than typically found for Ni_2P/SiO_2 catalysts and in good accord with active site densities following from particle size. The excess phosphorus results in mesopore blocking by unreduced phosphate species, impeding the accessibility of the Ni_2P active sites as probed by CO chemisorption. The catalysts exhibited lower hydrodesulfurization (HDS) but similar or somewhat higher hydrodenitrogenation (HDN) activities than reference alumina-supported NiMo or CoMo catalysts in simultaneous thiophene HDS and pyridine HDN, as well as parallel dibenzothiophene HDS and *ortho*-methyl aniline HDN hydrotreating reactions. In general, the intrinsic activities of the Ni_2P catalysts were higher than those of $Ni_{12}P_5$ catalysts. The activities of these phosphide catalysts were found to be stable or increasing with reaction time. X-ray photoelectron studies of reduced catalysts exposed to a sulfiding mixture suggest that this increase is due to *in situ* sulfidation of the nickel phosphide to nickel phosphosulfide. Thus, it seems reasonable that surface phosphosulfides form the active catalytic surface in these catalysts.

Keywords: Nickel phosphide; SBA-15; Hydrodesulfurization; Thiophene; Dibenzothiophene; Hydrodenitrogenation; Pyridine; *Ortho*-methyl aniline

1. Introduction

Environmental regulations require significant reductions in the sulfur and nitrogen levels of transportation fuels. Fulfilling these requirements necessitates the development of new hydrotreating catalysts. High-surface area supports are useful for the preparation of new catalytic materials. Recently, silica-supported transition-metal phosphides were proven to outperform traditional Co(Ni)–Mo/Al_2O_3 hydrotreating catalysts in model catalytic studies [1].

Generally, phosphates were used mainly as an additive to improve the catalytic properties of CoMo- and NiMo-based hydrotreating catalysts [2]. Carbon-supported nickel sulfide without molybdenum has proven to be an active hydrotreating catalyst [3]. Thiophene HDS and quinoline HDN activities tended to increase in the presence of phosphorus [4]. These promising results led to a systematic study of the hydrotreating activity of nickel (cobalt)–phosphorus (sulfur) [Ni(Co)–P(S)] compounds [5]. Unsupported Ni(Co)–P(S) model compounds and carbon-, silica-, silica–alumina-, alumina-, and NaY zeolite-supported Ni–P and Co–P catalysts were prepared, characterized, and evaluated in thiophene HDS [5,6] and quinoline HDN [5,7]. During pretreatment or at reaction conditions, all compounds (even $NiPS_3$ after severe sulfidation with H_2/H_2S under high pressure), and supported catalysts were transformed to Ni_2P (or Co_2P) and the beneficial effect of phosphorus introduction to their hydrotreating activities was attributed to the formation

* Corresponding author.
E-mail address: koranyi@chemres.hu (T.I. Korányi).

0021-9517/$ – see front matter
doi:10.1016/j.jcat.2007.10.012

of the phosphide [5–7]. Later, bulk transition-metal phosphides [8,9] as well as silica-supported nickel phosphides [9,10] and other transition-metal phosphides (MoP) [11] were found to be more active HDN catalysts. The silica-supported catalysts were prepared by pore-volume impregnation of nickel nitrate (or ammonium heptamolybdate) and ammonium phosphate solutions, and after drying and calcination at 623 K, the resulting oxidic precursors were reduced in hydrogen flow up to 823 K. Precursors with a P-to-Ni ratio of 0.5 yielded mainly $Ni_{12}P_5$, whereas preparing phase-pure silica-supported Ni_2P and MoP catalysts required a slight excess of phosphate in the impregnating solution (P/Ni = 0.65 and P/Mo = 1.2, respectively) [10,11].

The effects of metal phosphide weight loading, initial P/Ni ratios, and pretreatment conditions on the hydrotreating activities of silica-supported catalysts are not unequivocal in the literature. Optimum Ni_2P loadings for hydrotreating were found at around 18 wt% above low-surface area silica supports [12] and at 30 wt% above high-surface area silica supports [13]. To obtain the desired stoichiometry (phase pure Ni_2P), an excess of phosphate must be added, i.e. for the optimal initial P/Ni ratios, these are 0.65 [10], 0.8 [13], and 2 [14], respectively. For impregnation, aqueous solution of di-ammonium hydrogen phosphate is used as the phosphorus source in most cases [8–12,14], but sometimes it is replaced by ammonium di-hydrogen phosphate [13,15]. The latter solution is more acidic than the former one, which is advantageous in the case of co-impregnation, because the resulting metal phosphate salt solution is more stable at lower pH. Generally, however, consecutive impregnation steps are used, and the nickel nitrate (or ammonium heptamolybdate) solution is first added to the silica support, followed by drying and impregnation with the ammonium phosphate solution. The oxidic catalyst precursor is obtained after calcination and then reduced in hydrogen to the active phosphide catalyst. For further characterization, the catalyst may be passivated in a 0.5–1 vol% O_2 containing gas flow.

Recently, other supports, such as alumina [15,16], carbon [17,18], MCM-41 [19], USY [20], and HMS [21], also have been applied for phosphorus-containing hydrotreating catalysts. SBA-15 is a mesoporous silica composed of two-dimensional hexagonal arrays of channels typically 5–9 nm in diameter [22].

The objective of this work was to combine the described synthesis procedures to arrive at well-defined Ni_2P and $Ni_{12}P_5$ phases with SBA-15, which has high-surface area ordered mesoporous silica support to examine the effect of different phases of nickel phosphides on the hydrotreating. The catalytic materials are evaluated in parallel HDS and HDN reactions. Earlier [23], we studied Ni_2P and $Ni_{12}P_5$ containing SBA-15- and CMK-5-supported catalysts in parallel thiophene HDS and pyridine HDN reactions. Because the nanoporous carbon-(CMK-5-) supported nickel phosphides exhibited much lower catalytic activities and selectivities than the SBA-15 supported ones [23], we did not study carbon-supported catalysts in this work. We compared the structural and textural properties of SBA-15-supported nickel phosphide catalysts as well as their catalytic performance in combined thiophene HDS and pyridine HDN and combined dibenzothiophene HDS and *ortho*-methyl aniline HDN. The novelty of the present work is using a mesoporous silica support to give better dispersion and to clarify the nature of active sites for nickel phosphide catalysts.

2. Experimental

2.1. Materials

The preparation of the SBA-15 support has been described extensively elsewhere [22]. SBA-15 has a two-dimensional structure and was synthesized from sodium silicate with a triblock copolymer (P123), which was used as a structure-directing agent [22]. The specific surface area and pore volume of SBA-15 were 701 m^2/g and 0.90 cm^3/g, respectively. The chemicals used for catalyst preparation were $Ni(NO_3)_2{\cdot}6H_2O$ (NNA) and $(NH_4)H_2PO_4$ (AHP), which are Alfa Aesar Puratronic products with >99.99% purity.

2.2. Catalyst preparation

The SBA-15 support was dried at 393 K overnight. NNA (0.980 g for 1 g of support) and AHP (0.775, 0.310, or 0.194 g for P/Ni = 2, 0.8, or 0.5 for 1 g of support) were dissolved in distilled water and mixed in a common metal phosphate solution. Then 2 g of the SBA-15 support was impregnated with the diluted phosphate solutions by incipient wetness impregnation. The catalyst precursors were dried at 393 K overnight. The dried sample was pelletized with a press, ground, and sieved to 0.85–1.4 mm. The precursor sample was reduced in a hydrogen flow of 200 cm^3/min. Toward this end, the sample was heated in hydrogen to 623 K at a rate of 3 K/min, then to 873 K at a rate of 1 K/min and kept at this temperature for 1 h. Subsequently, the gas was changed to 2000 cm^3/min nitrogen, followed by cooling to room temperature in 0.5 h. Finally, the SBA-15-supported catalysts were passivated in a flow of 1 vol% O_2 in N_2 (total, 2100 cm^3/min) for 1 h at room temperature. The catalysts are designated by the support (SBA) and by the initial P/Ni ratios, which were 2 (high excess phosphorus, denoted by subscript H), 0.8 (excess P, denoted by subscript E), or 0.5 (stoichiometric P, denoted by subscript S) in the aqueous metal phosphate impregnation solutions. A list of the prepared catalysts with their Ni and P elemental composition as determined by inductively coupled plasma (ICP) measurements is given in Table 1.

2.3. Temperature-programmed reduction

A catalyst analyzer (BEL CAT, PCI 3135) was used for temperature-programmed reduction (TPR). The sample was placed in a cylinder-like quartz reactor situated in a furnace controlled by a temperature programmer (Yamatake SDI 15). The temperature of the sample was monitored by a thermocouple connected to the center of the reactor. Before reduction, the sample was pretreated in helium gas stream (30 cm^3/min flow rate, heating from 300 to 673 K at a rate of 5 K/min and maintained at 673 K for 2 h). The temperature of the sample was raised from 373 to 940 K at a rate of 1 K/min

Table 1
Physicochemical data of the various phosphide catalysts: BET surface areas (S_{BET}), total pore volumes, loadings, phases identified by XRD and corresponding crystallite sizes (d_{XRD}), P-containing phases detected by ^{31}P NMR, CO uptakes (n_{CO}), and estimated surface site concentration (n_{sites})

Catalyst	S_{BET} (m^2/g)	Pore volume (cm^3/g)	Ni (wt%)	P (wt%)	P/Ni molar ratio	XRD phases	d_{XRD} (nm)[a]	^{31}P NMR phases	n_{CO} (μmol/g)	n_{sites}[b] (μmol/g)
SBA_H	223	0.27	11.1	5.2	0.88	Ni_2P	41	$Ni_2P + PO_4^{3-}$	12	49
SBA_E	364	0.43	11.3	2.5	0.42	$Ni_2P + Ni_{12}P_5$	8 (Ni_2P)[c]	$Ni_2P + Ni_{12}P_5 + PO_4^{3-}$	17	–[d]
SBA_S	454	0.49	12.7	3.0	0.45	$Ni_{12}P_5$	17	$Ni_{12}P_5$	144	131

[a] Crystallite sizes determined from line broadening of the XRD patterns of passivated catalysts by the Scherrer equation.
[b] Calculated from the XRD particle size according to Ref. [14]; $n_{sites} = S_{eff} \cdot n \cdot C$ with S_{eff} the effective surface area of the nickel phosphide ($S_{eff} = 6/\rho d$ with ρ being the density of nickel phosphides taken as $\rho = 7.09$ g/cm^3 and n the average surface metal atom density $= 1.01 \times 10^{15}$ cm^{-2}) and C the fractional weight loading ($g_{nickel\ phosphide}/g_{cat}$).
[c] The crystallite size of the Ni_2P phase is 8 nm in the *in situ* reduced SBA_E sample.
[d] Metal site concentration is not calculated because the crystallite size of passivated SBA_E catalyst cannot be determined.

and kept there for 30 min in a 5% H_2/Ar gas stream (flow rate, 30 cm^3/min). The degree of reduction was measured using a four-element semi-diffusion thermal conductivity detector.

2.4. X-ray diffraction

X-ray diffractograms below $2\Theta = 3°$ were recorded on a Rigaku Multiflex instrument operated at 1.5 kW, using CuK_α radiation at 40 kV and 40 mA. X-ray diffraction (XRD) scanning was performed under ambient conditions at steps of 0.01° and an accumulation time of 1 s per step. *In situ* XRD patterns were obtained in the range of $2\Theta = 30$–60° on a Philips PW 1050 diffractometer using CuK_α radiation. The sample was reduced in a 70-cm^3/min hydrogen gas stream while being heated to 723 K at a rate of 3 K/min, followed by further heating to 773, 823, and 873 K at a rate of 1 K/min. At each of these temperatures, the sample was kept isothermal for 1 h, with an *in situ* XRD pattern recorded during the last 50 min. After the sample was cooled to room temperature under hydrogen gas stream, a final XRD pattern was recorded. The crystallite size was calculated from the full width at half maximum values derived from full profile fitting using Scherrer's equation with Warren's correction for instrumental line-broadening at $2\Theta = 40°$.

2.5. N_2 adsorption measurements

The nitrogen adsorption–desorption isotherms were measured at liquid nitrogen temperature (77 K) using a Quantachrome Autosorb-1MP volumetric adsorption analyzer. Before the measurements, the samples were outgassed under vacuum for 12 h at 473 K. The apparent specific surface areas were calculated from adsorption data obtained from the linear portion of Brunauer–Emmett–Teller (BET) plots ($P/P_0 = 0.1$–0.3). The total volume of micropores and mesopores was calculated from the amount of nitrogen adsorbed at $P/P_0 = 0.95$, assuming that adsorption on the external surface was negligible compared with adsorption in pores. The pore size distributions were calculated by analyzing the adsorption branch of the N_2 sorption isotherm using the Barret–Joyner–Halenda method.

2.6. ^{31}P nuclear magnetic resonance

^{31}P nuclear magnetic resonance (NMR) spectra were obtained on a Varian 400-MR spectrometer at 161.9 MHz. KH_2PO_4 was used to optimize the magic angle spinning (MAS) conditions and also as an external reference (+0.4 ppm relative to 85% H_3PO_4). The samples were placed in a 4-mm rotor and spun at 10 kHz. The spectra were acquired using a single 90-degree P-31 pulse (4 μs) under high-power proton decoupling conditions using composite pulses. The acquisition time varied between 40 and 25 ms, the recycle time was 1 s, and 10,000–40,000 scans were acquired.

2.7. Transmission electron microscopy

Transmission electron microscopy (TEM) experiments were carried out in a Philips Tecnai 10 microscope operated at 80–100 kV. The samples were dispersed in ethanol and placed on a carbon grid before TEM examinations.

2.8. CO chemisorption

Irreversible CO uptakes were usually measured over 60 mg of phosphide sample after re-reduction in hydrogen flow (50 cm^3/min) at 673 K for 2 h in a quartz reactor. After reduction, the catalyst was purged and cooled to room temperature in helium flow. CO was adsorbed on the samples in 3–4 Torr pressure steps in a 0–30 Torr pressure range. The total and physical CO adsorption isotherms were determined at room temperature, with the difference of the two isotherms considered the chemisorbed amount. The ratio of the surface Ni atoms was calculated from the quantity of chemisorbed CO molecules assuming 1:1 stoichiometry.

2.9. X-ray photoelectron spectroscopy

The X-ray photoelectron spectroscopy (XPS) measurements were carried out on a VG Escalab 200 setup with standard Al anode (Al$K_\alpha = 1486.3$ eV) operating at 300 W. The pressure during the measurements was around 10^{-9} mbar. The reference line for calibration was the C 1s line at 284.5 eV. The samples

were re-reduced in hydrogen for 2 h at 673 K, followed by sulfidation in a mixture of H_2S/H_2 (10 vol% H_2S) for 2 h at 673 K. After the samples were cooled to room temperature, they were transferred to a glovebox without being exposed to air. Samples were ground, pressed onto carbon film, and transferred to the XPS apparatus through a transfer facility to avoid air exposure.

2.10. Parallel thiophene HDS and pyridine HDN catalytic activities

The catalytic activity was evaluated in parallel HDS of thiophene and HDN of pyridine reactions in a stainless steel flow microreactor with fixed catalyst bed at 593 K and 20 bar overall pressure, as described in detail elsewhere [24]. The catalyst (sieve fraction 125–250 μm) was fixed in the reactor between two layers of glass wool. The catalyst amount (W) was varied between 20 and 60 mg. The feed contained 240 ppm of thiophene (TH) and 220 ppm of pyridine (PY) in H_2 at a total flow rate of 150 cm^3/min delivered by a tension pressure saturator. The rate of the feed, F, was kept constant. Each catalyst was tested at two space velocities (W/F) using different amounts of the fresh catalyst charge.

Before reaction, the phosphide catalysts were activated by *in situ* reduction in an H_2 stream at atmospheric pressure (25 cm^3/min) while being heated at a rate of 6 K/min to 673 K and held at this temperature for 2 h. After activation, the temperature was lowered to 593 K, and the gas flow was replaced by the feed mixture at 20 bar of pressure through a 6-port switching valve. Steady-state conversion was usually attained after 3–4 h on stream, and the representative conversions were calculated as average values from several subsequent analyses done over another 2–3 h. The feed and the reaction products were analyzed with an online gas chromatograph (HP 5890) equipped with a flame ionization detector and a packed glass column (3.5 m) filled with Carbopack B 60/80 4% Carbowax 20M (Supelco) operating isothermally at 398 K. The integral dependences of the conversions of individual components on space-time W/F were obtained for every catalyst. Tetrahydrothiophene was absent in the reaction mixture at our experimental conditions, and HDS gave only C_4 hydrocarbons and H_2S. In the HDN of pyridine, the amount of intermediate saturated amines (mostly piperidine, with traces of pentylamine) varied between 3 and 23%. The HDN reaction involved two consecutive irreversible steps: pyridine hydrogenation and piperidine (PI) hydrogenolysis. Both HDS and HDN reactions were described by pseudo-first-order kinetic equations. The catalyst activities are expressed by the rate constants for thiophene HDS (k_{TH}), pyridine hydrogenation (k_{PY}), and piperidine hydrogenolysis (k_{C5}). The rate constants correspond to the following equations [25] and were calculated by nonlinear regression from dependences of the conversions on W/F:

$$\text{for thiophene HDS:}\quad x_{TH} = x_{C4} = 1 - \exp[-k_{TH} W/F_{TH}],$$

$$\text{for pyridine HDN:}\quad x_{PY} = 1 - \exp[-k_{PY} W/F_{PY}],$$

$$x_{PI} = \frac{k_{PY}}{k_{C5} - k_{PY}}\left(\exp[-k_{PY} W/F_{PY}] - \exp[-k_{C5} W/F_{PY}]\right),$$

and

$$x_{C5} = 1 - \frac{k_{C5}}{k_{C5} - k_{PY}} \exp[-k_{PY} W/F_{PY}] + \frac{k_{PY}}{k_{C5} - k_{PY}} \exp[-k_{C5} W/F_{PY}],$$

where x is conversion, TH is thiophene, C4 are C_4 hydrocarbons, PY is pyridine, PI is piperidine, and C5 are C_5 hydrocarbons.

For comparison purposes, the catalytic activity of a commercial NiMo/alumina (Shell 324, 2.8 wt% Ni, 11.8 wt% Mo) was evaluated under the same experimental conditions (but instead of reduction, in situ sulfidation at 673 K for 2 h at atmospheric pressure in a mixture of 10% H_2S in H_2 was applied), as reported recently [24].

2.11. Parallel dibenzothiophene HDS and ortho-methyl aniline HDN catalytic activities

For the simultaneous dibenzothiophene (DBT) HDS and *o*-methyl aniline (OMA) HDN hydrotreating reactions, a 100-mg catalyst sample, sieved to a particle size of 125–250 μm, was diluted with 6 g of SiC to achieve isothermal plug–flow conditions in continuous mode in a fixed-bed reactor. To remove the oxygen from the surface, the catalyst was activated *in situ* in H_2 (at a flow rate of 100 cm^3/min at atmospheric pressure) at 673 K for 2 h (heating rate, 6 K/min). The reference $CoMo/Al_2O_3$ catalyst (Shell C444, 9.8 wt% Mo and 3.4 wt% Co) was activated in a 10 vol% H_2S-containing H_2 stream at a flow rate of 60 cm^3/min under the same conditions. After activation, the pressure was increased to 3.0 MPa and the temperature was decreased to 613 K for the hydrotreating reactions. The liquid reactant was fed into the hydrogen stream in the reactor at a rate of 500 cm^3/min with a speed of 0.1 cm^3/min using a high-pressure pump. The composition of the feed was 70 kPa *n*-decane, 1 kPa (400 ppm) *n*-heptane, 2.5 kPa (800 ppm) OMA, and 0.6 kPa (200 ppm) DBT. The reaction products were analyzed online with a HP 5890 gas chromatograph equipped with a CP Sil5-CB capillary column; *n*-decane and *n*-heptane were used as internal standards for the HDS and HDN reactions, respectively. The experiments were carried out for 12–15 h, with gas-phase samples taken every 45 min. Only biphenyl (BP) and cyclohexylbenzene (CHB) for DBT HDS and toluene (T) and methylcyclohexane (MCH) for OMA HDN were found as reaction products.

3. Results

3.1. Composition of reduced and sulfided catalysts

As generally found in previous studies [10,13,14], the final P/Ni ratios of the activated catalysts were lower than the ratios used in the precursor solutions (P/Ni = 2 [high excess, denoted by subscript H] or 0.8 [excess, denoted by subscript E] or 0.5 [stoichiometric, denoted by subscript S]; Table 1). In this way, Ni_2P (P/Ni = 0.5) and $Ni_{12}P_5$ (P/Ni = 0.42) were obtained,

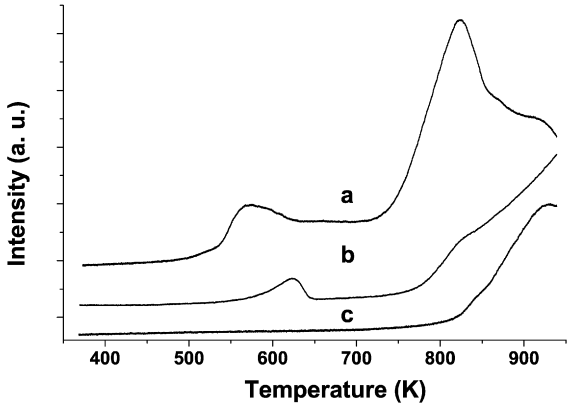

Fig. 1. TPR traces of SBA_S (a), SBA_E (b), and SBA_H (c) catalysts. Intensity is given in arbitrary unit (a.u.). Temperature range from 373 to 940 K, heating rate 1 K/min in a 5% H_2/Ar gas stream (flow rate 30 cm^3/min).

even though the SBA_H catalyst demonstrated a significant phosphorus excess (0.88). In contrast, elemental analysis of SBA_E (0.42) showed the presence of $Ni_{12}P_5$ when the phosphorus content of SBA_S (0.45) catalyst was intermediate between compositions corresponding to $Ni_{12}P_5$ and Ni_2P. The active phase composition also was determined after the combined thiophene HDS and pyridine HDN catalytic reaction; the compositional changes remained below 10% in these cases. The sulfur content of the SBA_S catalyst was determined after a sulfidation treatment at 673 K for 2 h and was found to be 0.8 wt% S.

3.2. TPR

The TPR profile comprises two main features, one at low temperature and one at higher temperature (Fig. 1). The first peak at around 600 K corresponds to the reduction of nickel oxides to metallic nickel [26]. The second peak is assigned to the formation of nickel phosphides [26] and/or the reduction of excess phosphate. The low-temperature peak shifted to higher temperature when going from SBA_S to SBA_E. This peak was not observed for SBA_H, presumably due to the effect of excess phosphate. The maximum of the second peak occurred at 823 K for SBA_S, but shifted to 933 K for SBA_H. The TPR profile for SBA_E indicates that the maximum of the second peak occurred beyond our experimental temperature limit (940 K). The 823 K peak appeared as a weak shoulder for the SBA_E and SBA_H samples.

3.3. XRD

The XRD patterns recorded at low angles (below $2\Theta = 3°$) demonstrate that all SBA-15-supported catalysts retained their original ordered structures almost completely (Fig. 2). Some deterioration of the structure could be seen, but the presence of higher index reflections indicated that the mesoporous structure was still intact.

The *in situ* XRD patterns recorded at high angles showed the presence of two phosphide phases, Ni_2P and/or $Ni_{12}P_5$, in the catalyst samples (Fig. 3, Table 1). Besides the final (873 K) curves, only those patterns are shown, which changed

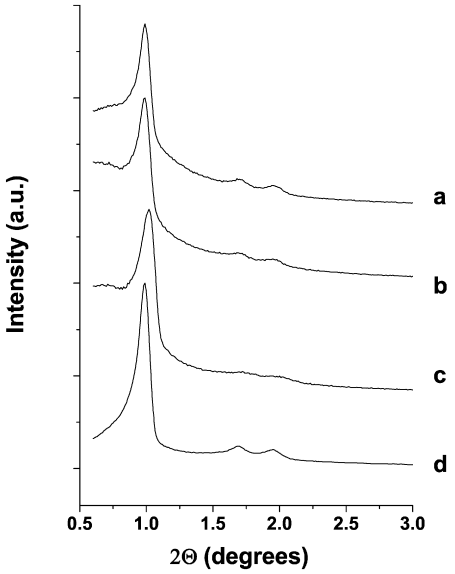

Fig. 2. XRD patterns of SBA_S (a), SBA_E (b), and SBA_H (c) catalysts and SBA-15 support (d) at low angle ($2\Theta < 3°$). Intensity is given in arbitrary unit (a.u.).

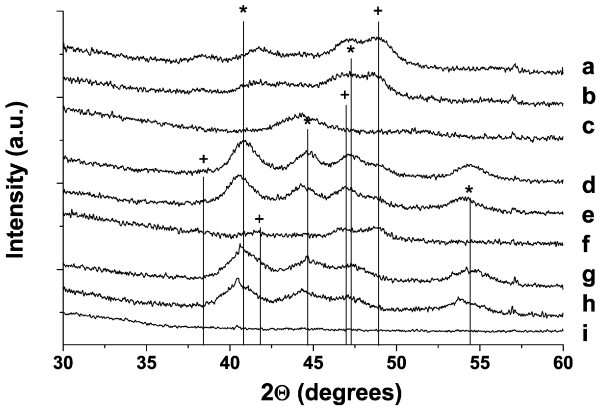

Fig. 3. *In situ* XRD patterns of the catalysts at high angle ($2\Theta > 30°$) during temperature-programmed reduction (3 K/min to 723 K, then 1 K/min to 773, 823, and 873 K, each temperatures kept for 1 h) in 30 cm^3/min hydrogen stream. Intensity is given in arbitrary unit (a.u.). Patterns of SBA_S at 873 (a), 773 (b), and 723 K (c), those of SBA_E at 873 (d), 823 (e), and 773 K (f), those of SBA_H at 873 (g), 823 (h), and 773 K (i). The four most intense lines of Ni_2P and $Ni_{12}P_5$ phases are designated by * and + symbols, respectively.

during the heating period compared with the previous pattern (except for SBA_H at 773 K; Fig. 3i). Crystalline phosphate phases were not identified. The characteristic peaks of metallic nickel at 44.4 and 51.8° [27] were observed only in the pattern of SBA_S at 723 K (Fig. 3c). At 773 K, only $Ni_{12}P_5$ appeared in the patterns of SBA_E (Fig. 3f) and SBA_S (Fig. 3b). A further increase to 823 K resulted in the presence of Ni_2P in the patterns of SBA_E (Fig. 3e) and SBA_H (Fig. 3h). For the SBA_S, SBA_E, and SBA_H samples, the pattern no longer changed after reduction at 773, 823, and 823 K, respectively. This indicates that the final nickel phosphide state was reduced for all samples well below 873 K. When a higher excess of phosphorus was used, only the Ni_2P phase was detected (SBA_H). The dominant phase in the stoichiometrically

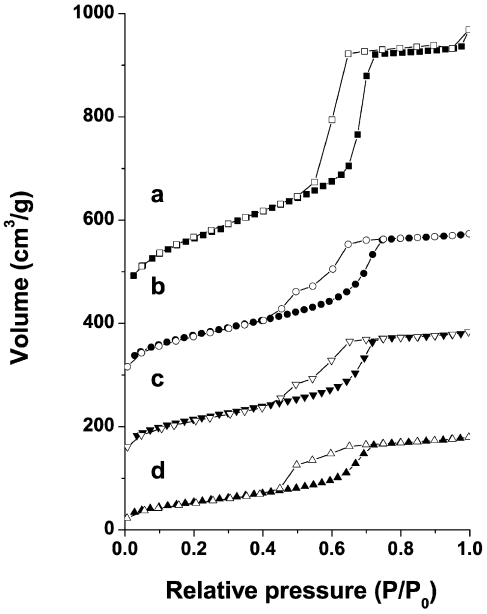

Fig. 4. Nitrogen adsorption–desorption isotherms of the SBA-15 support (a) and SBA_S (b), SBA_E (c), and SBA_H (d) catalysts at 77 K. The isotherms for SBA-15, SBA_S, and SBA_E are offset vertically by 350, 250, and 100 cm^3/g, respectively.

prepared sample (SBA_S) was $Ni_{12}P_5$. The XRD pattern of the SBA_E catalyst showed some broad peaks of both phosphide phases (Fig. 3), which contrasts with the stoichiometric P/Ni ratio of $Ni_{12}P_5$ (Table 1). The crystallite sizes of passivated catalysts calculated by Scherrer's equation were quite uniform (17–41 nm). The particle size of the passivated SBA_E catalyst could not be determined; however, a much smaller size (8 nm) was calculated from the pattern of the *in situ* reduced sample. The crystallite size calculated from Scherrer's equation is a mean value and does not represent the full size distribution.

3.4. N_2 porosimetry

The BET surface area and total pore volume of the parent SBA-15 support were 701 m^2/g and 0.90 cm^3/g, respectively. Table 1 indicates a very significant decrease in the specific surface areas and pore volumes of all catalysts on metal phosphide formation. The sorption isotherm of SBA-15 (Fig. 4a) exhibited a narrow hysteresis loop in the P/P_0 region of 0.53–0.72, due to capillary condensation in the cylindrical mesopores. Compared with the support, the nitrogen adsorption isotherms of the nickel phosphide catalysts (Fig. 4, b–d) showed a significant decrease in pore volume. The hysteresis loop was broader to 0.42 P/P_0 in the desorption branch. The average diameter of mesopores was around 7 nm (Fig. 5). It is also noteworthy that the pore size distribution of the nickel phosphide catalysts became less homogeneous with increasing phosphorus loading (Fig. 5). This indicates that some particles were situated inside the mesoporous structure, partially blocking the cross-section of the initial cylindrical pores. This pore-blocking effect was most conspicuous in the SBA_H sample (Fig. 5d).

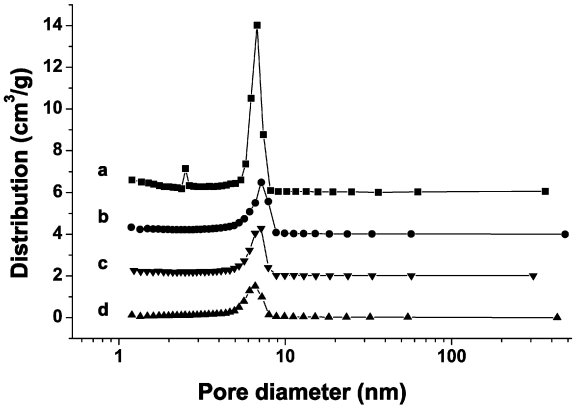

Fig. 5. Pore size distributions of the SBA-15 support (a), and SBA_S (b), SBA_E (c), and SBA_H (d) catalysts calculated from the sorption isotherms. The distributions for SBA-15, SBA_S, and SBA_E are offset vertically by 2, 4, and 6 cm^3/g, respectively.

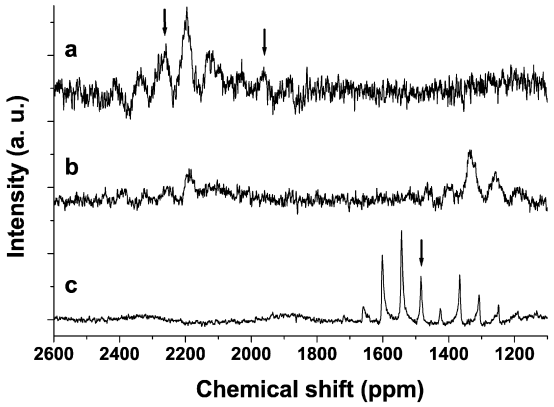

Fig. 6. Nickel phosphide region (2600–1100 ppm) in the ^{31}P NMR spectra of SBA_S (a), SBA_E (b), and SBA_H (c) catalysts. Intensity is given in arbitrary unit (a.u.). The isotropic signals are indicated by arrows.

3.5. ^{31}P NMR

^{31}P NMR was used to confirm the presence of crystalline phases identified by XRD. Unlike XRD, this method is not restricted to the identification of larger crystallites. Generally, Ni_2P supported on silica exhibited two sideband patterns with isotropic chemical shifts at 4081 and 1487 ppm [10]. Centerbands for $Ni_{12}P_5$ on SiO_2 were located at 2259 and 1941 ppm, respectively [10]. In the present case, the isotropic phosphide signals were observed at 4071 and 1484 ppm for SBA_H and at 2259 and 1962 ppm for SBA_S (Fig. 6). Accordingly, the Ni_2P region (1100–1700 ppm) in ^{31}P NMR spectra contained features of the catalysts prepared by P excess only. The resonances in the $Ni_{12}P_5$ region (1800–2600 ppm) were quite weak for SBA_S and even weaker for SBA_E. At the same time, Ni_3P could not be identified in any of the studied catalysts. At least four different phosphate signals with intense signal structures due to paramagnetic phosphate species [28] were present in the ^{31}P NMR spectra of SBA_H and SBA_E at chemical shifts of between +4 and −40 ppm (Fig. 7). The signals at around +4, −6, and −18 ppm can be assigned to $H_nPO_4^{(3-n)-}$, $P_2O_7^{4-}$, and $(PO_3^-)_n$ species, respectively [29,30]. The peak at around −35 ppm can be assigned to silicon phosphates in a paramagnetic (Ni) sur-

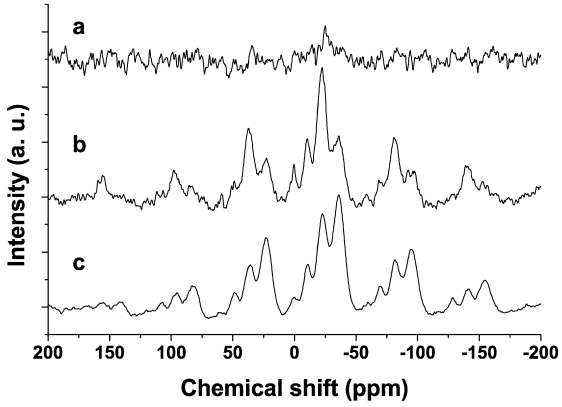

Fig. 7. Phosphate region (200 to −200 ppm) in the ^{31}P NMR spectra of SBA_S (a), SBA_E (b), and SBA_H (c) catalysts. Intensity is given in arbitrary unit (a.u.).

rounding [31]. The presence of a range of phosphate species was likely related to the passivation procedure, which resulted in the reoxidation of some nickel phosphide particles. Moreover, some unreduced phosphate species [11] were present due to the excess phosphorus in the SBA_H and SBA_E samples. The NMR spectrum of the catalyst prepared with the stoichiometric phosphorus content (SBA_S) provides a minor indication of the presence of a very weak phosphate signal around −25 ppm (Fig. 7a).

3.6. TEM

Distinct differences in the morphologies and particle sizes of the samples can be seen in the TEM images (Fig. 8). The TEM image of SBA_H (Fig. 8a) shows larger nickel phosphide particles than that of SBA_S (Fig. 8b). The particle size distribution of SBA_S (Fig. 8b) appears to be more homogeneous than that of SBA_H (Fig. 8a). The typical pattern of the hexagonal SBA-15 structure with a diameter of straight 8-nm [32] pores can be clearly seen in the micrograph of the SBA_S catalyst (Fig. 8b) in agreement with the 7 nm average pore size diameters (Fig. 5). In contrast, the pore structure of SBA_H sample (Fig. 8a) cannot be clearly distinguished, presumably due to the presence of phosphate (Table 1, Fig. 7). In contrast to the typical stacked morphologies of Mo and W sulfides, phosphides are not layered and form spherical particles that can be well dispersed on supports [20]. Particles form aggregates on both supports; particle size ranged from approximately 3 to 25 nm, similar to the 5–30 nm Ni_2P particles observed on silica supports [13,33]. Larger agglomerates of nickel phosphides were present on the external surfaces of the support grains (Fig. 8a), and some particles were well distributed in the support mesopores (Fig. 8b). The large (25 nm) particles derived from TEM (Fig. 8) and those calculated from XRD (17–41 nm) are in reasonable agreement.

3.7. CO chemisorption

Phosphide sites can be titrated by CO chemisorption at room temperature [1]. Irreversible CO uptake measurements were used to titrate the surface metal atoms and to provide an estimate of the active sites on the catalysts [14]. The measured

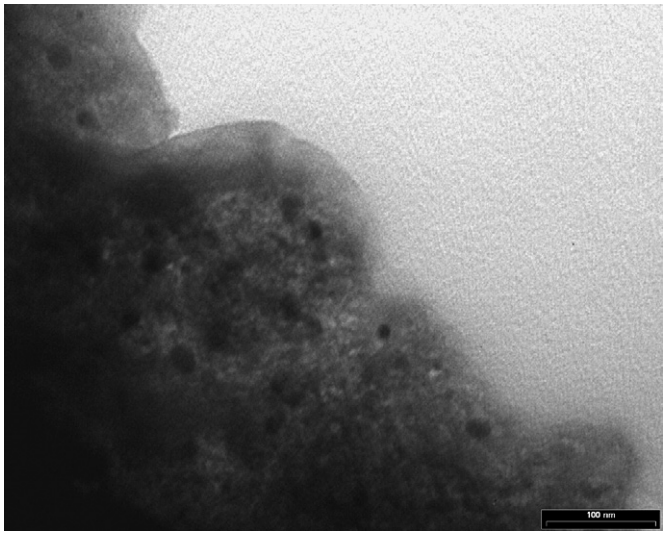

(a)

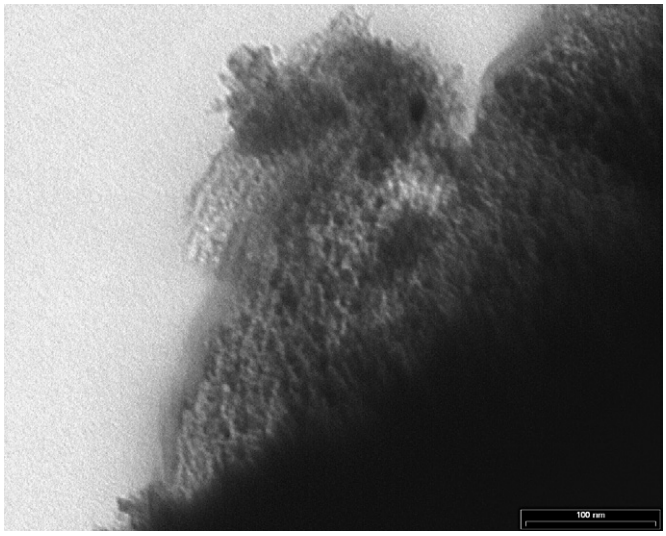

(b)

Fig. 8. Transmission electron micrographs of SBA_H (a) and SBA_S (b) samples.

CO adsorption capacities (S) are presented in Table 1. The active site density of the SBA_S catalyst (144 μmol/g_{cat}) was three times higher than the highest value (49 μmol/g_{cat}) reported for Ni_2P/SiO_2 catalysts in the literature [14].

The considerable lower CO uptakes of SBA_E and SBA_H catalysts indicate that their surface is blocked by phosphates, which prevents adsorption [14] and therefore it is suggested that reliable crystallite sizes cannot be calculated from CO chemisorption [33]. The possibility of blocking by phosphate species for the excess phosphorus samples is in accordance with the NMR and TEM results. Phosphate species can be identified in the NMR spectra of these samples (Fig. 7); moreover, the pore structure cannot be clearly distinguished in the TEM image of the SBA_H catalyst (Fig. 8a).

3.8. X-ray photoelectron spectroscopy

XP spectra in the Ni(2p) and P(2p) regions for the reduced and sulfided SBA-15-supported catalysts are shown in Fig. 9.

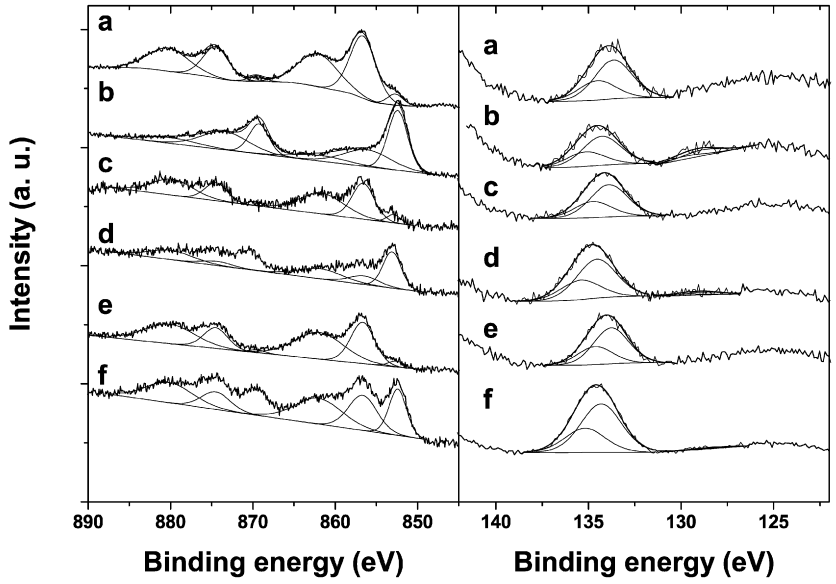

Fig. 9. X-ray photoelectron spectra in the Ni 2p and P 2p regions for reduced and sulfided (SUL) SBA-15-supported catalysts: SBA_S (a), SBA_S SUL (b), SBA_E (c), SBA_E SUL (d), SBA_H (e), and SBA_H SUL (f). Intensity is given in arbitrary unit (a.u.).

Table 2
XPS binding energies (BE, eV) and relative concentrations (X = Ni + P + S) for the reduced and sulfided (SUL) SBA-15-supported catalysts

Sample	Ni $2p_{3/2}$	Ni satellite	Ni $2p_{1/2}$	Ni satellite	P 2p	P 2p	$\frac{Ni^{\delta+}/\sum Ni}{P^{\delta-}/\sum P}$	Ni/X	P/X	Ni/P	$\frac{X/Si}{S/X}$
SBA_H	852.6		869.5				0.034	0.670	0.330	2.031	0.151
	856.7	861.9	874.5	880.1	133.8	134.6	0				
SBA_E	852.9		869.7				0.058	0.445	0.555	0.800	0.085
	856.6	861.6	874.5	879.8	133.9	134.8	0				
SBA_S	852.7		869.6				0.053	0.804	0.196	4.11	0.180
	856.6	862.1	874.5	880.3	133.7	134.5	0				
SBA_H	852.4	856.2	869.3	873.4	128.1	129.0	0.381	0.410	0.590	0.696	0.234
SUL	856.7	862.0	874.5	880.2	134.3	135.2	0.019				
SBA_E	853.1	856.9	870.0	874.1	128.8	129.7	0.597	0.403	0.509	0.793	0.182
SUL	856.5	861.8	874.4	880.0	134.6	135.4	0.068				0.088
SBA_S	852.4	856.2	869.3	873.4	128.8	129.7	0.850	0.687	0.252	2.73	0.132
SUL	856.7	861.8	874.6	880.0	134.3	135.2	0.170				0.061

The binding energies and relative surface atomic ratios calculated from the band intensities are presented in Table 2. All spectra were decomposed taking into account the spin-orbital splitting of Ni $2p_{3/2}$ and Ni $2p_{1/2}$ lines (17 eV) and the presence of satellite peaks at about 5 eV higher than the binding energy of the parent signal [34]. The bands at 856.5–856.7 eV and at 133.7–135.4 eV are assigned to Ni^{2+} and P^{5+} (phosphate) species, respectively (BEs in bottom lines in Table 2). Some spectra signals at 852.4–853.1 eV and at 128.1–129.7 eV were observed, which are assigned to $Ni^{\delta+}$ and $P^{\delta-}$ species, respectively (BEs in top lines in Table 2). These binding energies are in good agreement with the Ni $2p_{3/2}$ and P 2p values reported in unsupported Ni_2P and $Ni_3(PO_4)_2$ (857.1 and 133.9 eV, respectively [6]) as well as in SiO_2-supported $Ni_{12}P_5$ (856.8 eV for Ni^{2+}, 853.0 eV for $Ni^{\delta+}$, and 133.8 eV for P^{5+} [15]) and Ni_2P (857.2 eV for Ni^{2+}, 853.5 eV for $Ni^{\delta+}$, 134.3 eV for P^{5+}, and 129.5 eV for $P^{\delta-}$ [13]) catalysts.

Only around 5% of the observed surface nickel atoms were in the reduced $Ni^{\delta+}$ state in the reduced catalysts, but their contribution increased to 38% in SBA_H, 60% in SBA_E, and 85% in SBA_S in the sulfided (SUL) samples. In parallel, the concentration of reduced $P^{\delta-}$ species also increased from zero in the reduced samples to 2% in SBA_H SUL, 7% in SBA_E SUL, and 17% in SBA_S SUL, indicating that at least part of $Ni^{\delta+}$ and all of the $P^{\delta-}$ species are constituents of the same phase.

The surface Ni and P concentrations for the reduced SBA_H catalyst corresponded to the bulk composition of Ni_2P, in agreement with the XRD result. This finding did not hold for the other catalysts, possibly due to the significant changes in surface active-phase dispersion (X/Si ratios varying from 8.5 to

Table 3
Results for parallel thiophene HDS and pyridine HDN over mesoporous silica-supported nickel phosphides and an alumina-supported NiMo sulfide reference catalyst. First-order rate constants for thiophene (TH) HDS (k_{TH}), pyridine (PY) hydrogenation (k_{PY}), and piperidine hydrogenolysis (k_{C5}) are given ($T = 593$ K, $P = 20$ bar)

Catalyst	Thiophene HDS		Pyridine HDN			
	k_{TH} (mol/(kg$_{cat}$ h))	k_{TH} (mol/(mol h))[a]	k_{PY} (mol/(kg$_{cat}$ h))	k_{PY} (mol/(mol h))[a]	k_{C5} (mol/(kg$_{cat}$ h))	k_{C5} (mol/(mol h))[a]
SBA_H	1.5	130 (31[b])	1.7	148 (35[b])	6.9	599 (142[b])
SBA_E	1.6	97	2.0	121	7.6	460
SBA_S	2.8	19	3.2	22	29.9	207
$NiMo/Al_2O_3$[c]	8.1	–	2.5	–	6.1	–

[a] Calculated from the value obtained from CO chemisorption (n_{CO}).
[b] Calculated from the dispersion (n_{sites}).
[c] $NiMo/Al_2O_3$ reference catalyst, data taken from Ref. [24].

23.4%). The undetectable (SBA_H SUL) and very small surface S concentrations of SBA_E SUL (9%) and SBA_S SUL (6%) catalysts (Table 2) were in good agreement with our previous results [6]; accordingly, the surface S content of sulfided unsupported Ni_2P and $Ni_3(PO_4)_2$ was 3 and 9%, respectively. The low bulk sulfur content of SBA_S SUL catalyst (0.8 wt%) also supports the low surface sulfidability of SBA-15-supported nickel phosphide catalysts.

The surface active-phase composition of sulfided SBA_S catalyst was $Ni_{2.7}P_{1.0}S_{0.24}$, which fits very well with the particle composition of $Ni_{2.4}P_{1.0}S_{0.24}$ for a sulfided $Ni_{12}P_5/SiO_2$ catalyst [15]. But the surface active phase composition of sulfided SBA_E catalyst was $Ni_{0.8}P_{1.0}S_{0.17}$, which does not fit with the compositions of sulfided $Ni_{12}P_5/SiO_2$ or sulfided Ni_2P/SiO_2 ($Ni_{2.0}P_{1.0}S_{0.017}$) catalysts [15].

3.9. Parallel thiophene HDS and pyridine HDN catalytic activities

Table 3 summarizes the catalytic activities as pseudo-first-order reaction rate constants for the nickel phosphide catalysts and a reference $NiMo/Al_2O_3$ catalyst. The activities were nearly constant during the reaction, and no deactivation was observed during the first 200 min. The metal phosphide catalysts had a lower thiophene HDS reaction rate constant (k_{TH}) than the reference catalyst. The SBA-15-supported catalysts had similar pyridine hydrogenation (k_{PY}) and generally higher piperidine hydrogenolysis (k_{C5}) activities than the reference NiMo catalyst expressed per unit catalyst mass. The reaction rate constants are also expressed per mol metal site (Table 3).

3.10. Parallel DBT HDS and OMA HDN catalytic activities and selectivities

The nickel phosphide catalysts displayed catalytic activity in the HDS of DBT (Fig. 10) and the HDN of OMA (Fig. 11). The HDS activities of SBA_H and SBA_S catalysts increased with reaction time, whereas the initial activity of SBA_S was higher and increased less with time on stream. The HDN activity of SBA_E showed a significant activity increase (from 6% to >10%) compared with that of the other samples. The SBA_S catalyst displayed the highest HDS and HDN activities on a per-unit catalyst mass basis, but at the end of the reaction, the

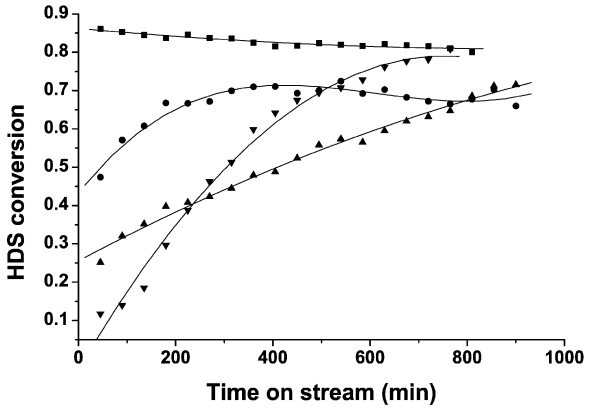

Fig. 10. HDS conversion of dibenzothiophene (DBT) as a function of time on stream over SBA_S (●), SBA_E (▼), SBA_H (▲), and a reference $CoMo/Al_2O_3$ (■) catalyst during simultaneous HDS of DBT and HDN of OMA at 613 K and 30 bar.

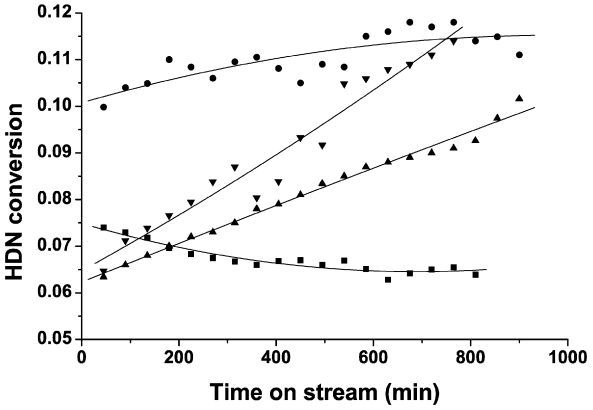

Fig. 11. HDN conversion of *o*-methylaniline (OMA) as a function of time on stream over SBA_S (●), SBA_E (▼), SBA_H (▲), and a reference $CoMo/Al_2O_3$ (■) catalyst during simultaneous HDS of DBT and HDN of OMA at 613 K and 30 bar.

activity of SBA_H reached approximately similar HDS and HDN levels as SBA_S (Figs. 10 and 11).

The initial pseudo-first-order reaction rate constants for DBT HDS and OMA HDN are given in Table 4. These values most closely reflect the activities of the nickel phosphide phases. Clearly, the catalytic activity on a per unit catalyst mass basis increased with decreasing phosphorus excess; therefore, this activity was the highest for the SBA_S catalyst prepared with

Table 4
Results for parallel dibenzothiophene (DBT) HDS and *o*-methyl aniline (OMA) HDN over mesoporous silica-supported nickel phosphides and an alumina-supported CoMo sulfide reference catalyst. Initial pseudo first-order rate constants for DBT HDS (k_{DBT}) and OMA HDN (k_{OMA}) are given ($T = 613$ K, $P = 30$ bar)

Catalyst	DBT HDS		OMA HDN	
	k_{DBT} (mol/(kg$_{cat}$ h))[a]	k_{DBT} (mol/(mol h))	k_{OMA} (mol/(kg$_{cat}$ h))[d]	k_{OMA} (mol/(mol h))
SBA_H	0.7	63[b] (15[c])	0.7	57[e] (14[f])
SBA_E	0.3	19[b]	0.7	40[e]
SBA_S	1.6	11[b]	1.1	7.3[e]
$CoMo/Al_2O_3$	4.4	–	0.7	–

[a] k_{DBT} (mol/(kg$_{cat}$ h)) $= XQ_{DBT}$, where X is the initial conversion, Q is the molar rate of the reactant.
[b] k_{DBT} (mol/(mol h)) $= XQ_{DBT}/n_{CO}$, where n_{CO} is the CO uptake (from Table 1).
[c] k_{DBT} (mol/(mol h)) $= XQ_{DBT}/n_{sites}$, where n_{sites} is the estimated surface site concentration (from Table 1).
[d] k_{OMA} (mol/(kg$_{cat}$ h)) $= XQ_{OMA}$.
[e] k_{OMA} (mol/(mol h)) $= XQ_{OMA}/n_{CO}$.
[f] k_{OMA} (mol/(mol h)) $= XQ_{OMA}/n_{sites}$.

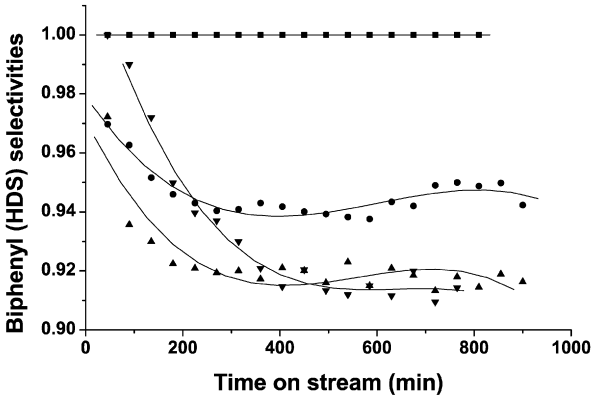

Fig. 12. Biphenyl product selectivities of DBT HDS over SBA_S (●), SBA_E (▼), SBA_H (▲), and a reference $CoMo/Al_2O_3$ (■) catalyst during simultaneous HDS of DBT and HDN of OMA at 613 K and 30 bar.

initial stoichiometric P content. The HDS activities were comparable to that of the reference $CoMo/Al_2O_3$ catalyst, whereas the HDN activities of the metal phosphide catalysts were generally higher.

The selectivities to biphenyl and cyclohexylbenzene of all catalysts were quite similar at around 95% BP and 5% CHB (Fig. 12). In contrast, the OMA HDN selectivities (Fig. 13) varied among the catalysts. Toluene and MCH selectivities for the SBA_S catalyst were almost identical (55–60% and 40–45%, respectively) and did not change with reaction time. The toluene selectivities for SBA_E and SBA_H decreased significantly during the reaction and reached the same low level (<60%) at the end of the reaction as that for SBA_S (Fig. 13).

The OMA HDN conversion of the SBA_S catalyst was close to 10%, and those of SBA_H and SBA_E catalysts reached or exceeded this value at the end of the reaction (Fig. 11). The toluene (HDN) selectivity of the SBA_S catalyst was close to 60% and did not change during the reaction. The T selectivities of SBA_H and SBA_E samples were close to this value at

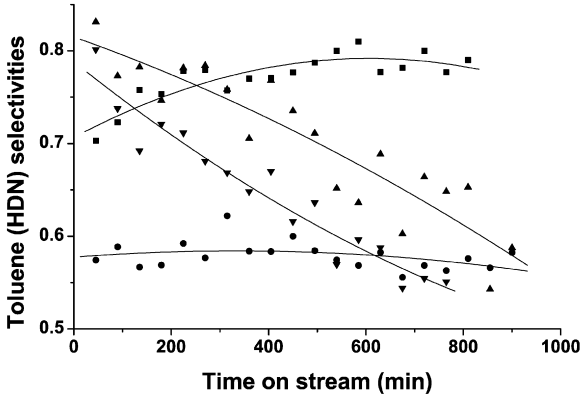

Fig. 13. Toluene product selectivities of OMA HDN over SBA_S (●), SBA_E (▼), SBA_H (▲), and a reference $CoMo/Al_2O_3$ (■) catalyst during simultaneous HDS of DBT and HDN of OMA at 613 K and 30 bar.

long reaction times (Fig. 13). Based on these findings, it may be concluded that the surface state of SBA-15-supported catalysts was similar at long time on stream and differed from the active sites in the CoMo reference catalyst.

In summary, SBA_S was shown to be already an active HDN catalyst after activation. The HDS activities of SBA_S and SBA_H increased with time on stream. The HDS and HDN activities of SBA_H both increased significantly during the reaction, and the HDN selectivity became close to that observed for SBA_S at longer time on stream.

4. Discussion

4.1. Active-phase composition

It is generally accepted that Ni_2P is the active phase in silica-supported nickel phosphide catalysts [1,5–7]. Nickel-rich phosphides exhibit much higher HDS activity than phosphorus-rich compositions over siliceous MCM-41, and Ni_2P/MCM-41 has been reported to be the most active catalyst in the HDS of dibenzothiophene [19]. In the present study, the catalysts containing predominantly $Ni_{12}P_5$ showed higher HDS and HDN activities compared with those catalysts with Ni_2P as the main nickel phosphide active phase. An important and striking difference between the catalysts prepared with a stoichiometric ratio ($Ni_{12}P_5$) and those with higher phosphorus amounts in the final catalyst is the significantly lower surface area and pore volume, as well as less homogeneous pore size distribution of the resulting catalysts. Indeed, Table 1 clearly shows that the surface area and pore volume of the SBA-15-based catalysts decreased significantly with increasing phosphorus loading. The NMR results indicate the presence of increasing amounts of phosphate groups. The smaller surface area was not due to the deterioration of the ordered mesoporous structure, as demonstrated by the low-angle XRD reflections. Consequently, we argue that the loss of surface area was due to blocking of mesopores by phosphate groups. As a result of the smaller surface area of phosphate-containing catalysts, the $Ni_{12}P_5$ particles in SBA_S were smaller than the Ni_2P particles in SBA_E and SBA_H. The broader NMR signals of the $Ni_{12}P_5$ are in accordance with this

difference. Thus, we tentatively attribute the greater activity of the $Ni_{12}P_5$ phase in SBA_S to its higher dispersion compared with the Ni_2P phase when the catalysts are prepared with an excess of phosphorus.

Two time-resolved XRD studies of the oxidic precursors by reduction in hydrogen revealed the formation of crystalline phases in Ni_2P/SiO_2 catalysts [26,35]. Accordingly, NiO was reduced to metallic Ni at around 500–700 K [26] or near 673 K [35] in the first step. Either Ni_2P was produced directly in the second step at 700–850 K [26] or $Ni_{12}P_5$ started to form at 823 K, followed by Ni_2P at 873 K. The final step was the reduction of phosphates at around 973 K [35]. Ni_2P formation is difficult in supported catalysts when $Ni_{12}P_5$ forms first, because the two crystal structures are very different [10]. The formation of metallic nickel was observed at around 600–723 K in the separate TPR and *in situ* XRD studies in the precursor of the SBA_S sample. $Ni_{12}P_5$ started to form at around 773–823 K in the precursors of SBA_S and SBA_E (Figs. 1 and 3). Ni_2P formation started at around 823 K in the precursors of SBA_H and SBA_E, but did not form from $Ni_{12}P_5$ (Figs. 1 and 3). The formation of Ni_2P and the reduction of excess phosphates could not be separated from the TPR traces. Because the maximum of the second TPR profile (Fig. 1) was at least 60 K higher in the precursors of SBA_H and SBA_E compared with the reduction temperature during catalyst preparation (873 K), incomplete reduction of the nickel phosphates in these passivated catalysts cannot be ruled out. $Ni_{12}P_5$, $Ni_{12}P_5 + Ni_2P$, and Ni_2P active phases likely were present in the passivated SBA_S, SBA_E, and SBA_H catalysts, respectively.

Despite the separated $Ni_{12}P_5$ and Ni_2P active phases in the passivated samples, the DBT HDS (Fig. 10) and OMA HDN (Fig. 11) conversions of SBA-15-supported catalysts approached each other during the reaction, indicating some common active phase that is neither $Ni_{12}P_5$ nor Ni_2P. This common active phase is most likely a phosphosulfide one. Previously, we identified the presence of a "special phosphosulfide" compound in freshly prepared $NiPS_3$ by XPS [5,6]. However, on sulfidation, this compound disappeared from the spectra. Sulfidation decreased the surface sulfur content as probed by XPS of this and other phosphosulfide model compounds [5,6]. Oyama et al. [12] identified a surface phosphosulfide phase by XRD and EXAFS on top of a Ni_2P core and suggested that this was a possibly active phase of Ni_2P/SiO_2 catalysts. The maximum sulfur level was suggested to be 5 mol% of the P content. In contrast to this, by DFT calculations, Nelson et al. [36] studied the replacement of up to 50% of surface phosphorus of bulk Ni_2P to sulfur and suggested that surface Ni_3PS is the actual active phase of Ni_2P for hydrotreating reactions.

The XPS spectra of sulfided catalysts (Fig. 9) clearly show a much higher proportion of nickel atoms in a $Ni^{\delta+}$ oxidation state compared with that of phosphorus atoms in a $P^{\delta-}$ state. The ratio of these species ($Ni^{\delta+}/\sum Ni$ and $P^{\delta-}/\sum P$) was very different in the three sulfided catalysts (Table 2). As outlined in Section 3.8, the surface active phase composition as probed by XPS of the sulfided SBA_S catalyst was $Ni_{2.7}P_{1.0}S_{0.24}$, which fits reasonably well with the bulk active phase composition, $Ni_{2.2}P_{1.0}S_{0.26}$, determined by elemental analysis. Such compositions correspond to the composition of the $Ni_{2.4}P_{1.0}S_{0.24}$ phase identified for a sulfided $Ni_{12}P_5/SiO_2$ catalyst [15]. Because the HDS and HDN conversions of SBA-15-supported catalysts resemble to each other in the final state of the hydrotreating reactions (Figs. 10 and 11), the presence of such a phosphosulfide active phase seems to be a reasonable explanation.

4.2. CO chemisorption

The number of active nickel sites as determined by CO chemisorption [14], n_{CO}, are summarized in Table 1. These data show very large differences in the active site densities. The CO chemisorption number varied from 12 to 144 μmol/g_{cat}. Values of 13 to 49 μmol/g_{cat} for Ni_2P/SiO_2 catalysts have been reported in the literature [14,37], which is the highest CO uptake found for catalysts prepared with an initial stoichiometric Ni/P ratio. With the present set of catalysts, low CO chemisorption active site densities were obtained when an excess of phosphorus was used. As outlined below, more extensively, the low CO chemisorption values may be due to blocking of the pores by the resulting phosphate species. As an alternative to the determination of active site density via CO chemisorption, we calculated the number of sites from the average particle size as determined from the XRD line-broadening of passivated catalysts. The number of sites, n_{sites}, is given by $S_{eff} \cdot n \cdot C$, where S_{eff} is the effective surface area of the nickel phosphide, n is the average surface metal atom density equaling 1.01×10^{15} cm^{-2}, and C is the fractional weight loading ($g_{nickel\ phosphide}/g_{cat}$). S_{eff} is calculated by $S_{eff} = 6/\rho d$ assuming cubic or spherical geometry of the nickel phosphide particles [14,26], with ρ representing the density of nickel phosphides, taken here as $\rho = 7.09$ g/cm^3. The corresponding results are also given in Table 1.

Comparison of the active site densities determined by CO chemisorption and the particle size indicates that, within the limits of experimental error, the values were similar for the SBA_S catalyst (144 and 131 μmol/g, respectively). In contrast, the CO chemisorption value for the SBA_H catalyst was substantially lower than that determined from the particle size (12 and 49 μmol/g, respectively). This indicates that for the SBA_H sample, the residual unreduced phosphate species plugged up to three-quarters of the active sites. Similarly, Wang et al. [26] reported a much lower CO uptake for a Ni_2P/SiO_2 catalyst compared with the expected value. The lesser extent of pore plugging for the porous SiO_2 catalyst is likely due to the more restricted average pore diameter of the mesoporous silica support used in this study.

4.3. Placement of the active phases

The relatively high CO chemisorption value for the SBA_S sample compared with values reported for silica-supported nickel phosphides [14,37] indicates that the use of an ordered mesoporous silica support resulted in improved dispersion of the nickel phosphide phase. As such, a considerable part of the nickel phosphide phase should be located inside the mesopores. The low-angle XRD patterns provide evidence that the

ordered mesoporous structure of the catalysts remained intact. The nitrogen adsorption isotherms and pore size distributions indicate that some particles were residing inside the structure and blocked some of the pores. TEM images and pore size distribution curves reveal a more homogeneous particle size distribution in SBA_S than in SBA_H. Phosphates were not identified in the SBA_S catalyst, but the BET surface areas of all catalysts were lower than those of the supports. This indicates that the nickel phosphide phases were located inside the mesopores. The specific surface areas of the catalysts containing excess phosphates were much lower than that of the SBA_S catalyst; this is taken as a strong indication of pore plugging. Moreover, in these catalysts, the particle size is large, and it can be argued that the nickel phosphide particles are located mainly outside the mesopores. In the SBA_H catalyst, the phosphate species were clearly blocking the mesopores and decreasing CO uptake. SBA_E with excess phosphorus also contained a quite widely dispersed mixture of Ni_2P and $Ni_{12}P_5$ phases, but, similar to SBA_H, the remaining phosphate species were clearly blocking the mesopores. We did not calculate a number for n_{sites}, because the XRD patterns did not allow accurate determination of the particle size of the $Ni_{12}P_5$ phase.

In summary, a large part of the $Ni_{12}P_5$ phase was present in well-dispersed form inside the mesopores of SBA-15 when a stoichiometric amount of phosphorus was used in the syntheses. Increasing the amount of phosphorus to induce the formation of Ni_2P had a negative effect on the accessibility of the active phase, because the remaining unreduced phosphate species blocked the mesopores.

4.4. Parallel HDS and HDN reactions

The pseudo-first-order reaction rate constants for parallel thiophene HDS and pyridine HDN reactions and parallel DBT HDS and OMA HDN reactions are reported in Tables 3 and 4, respectively. In general, compared with reference CoMo and NiMo sulfide catalysts supported on alumina, the HDS activities of the nickel phosphide catalysts were somewhat lower, whereas the HDN activities were almost the same order of magnitude or higher (SBA_S). Moreover, on the same basis, the $Ni_{12}P_5$-containing catalysts exhibited higher activity than the Ni_2P-based ones. On the other hand, the dispersion measurements indicated substantial differences between these catalysts. To account for such differences, the first-order reaction rate constants were recalculated on the basis of the number of accessible sites. Toward this end, the values for the CO uptake were used following the argument that sites that are not accessible for CO also will not be accessible for the larger reactants used in the present work. Because the catalysts prepared with excess phosphorus exhibited a discrepancy between the active site density based on CO chemisorption and that based on the particle size, the first-order reaction rate constants were also expressed on the basis of particle size active site density (n_{sites}). These intrinsic reaction rate constants based on CO chemisorption indicated that catalysts containing predominantly Ni_2P phases were more active than those containing $Ni_{12}P_5$ phases. For the SBA_E catalyst, which contained a mixture of Ni_2P and $Ni_{12}P_5$ due to the smaller excess of phosphorus used in its preparation compared with the synthesis of SBA_H, the activities in the various reactions were intermediate between those of SBA_S ($Ni_{12}P_5$) and SBA_H (Ni_2P). The higher activity of the Ni_2P over the $Ni_{12}P_5$ phase was in accord with recent reports [14,15,38]. For the parallel DBT HDS and OMA HDN, substantial increases of the reactivity were observed with time on stream. As shown earlier by others [1,12–15,36], this activity increase was most likely due to sulfidation of the surface of the nickel phosphide phase to a nickel phosphosulfide, which agrees with the aforementioned findings of sulfur incorporation in a spent sample.

The reliability of calculated intrinsic activities can be compared with data published in the literature. A TOF of 0.017 s^{-1}, calculated from O_2 chemisorption capacities for thiophene HDS over Ni_2P/SiO_2 catalysts [13], is equivalent to $k_{TH} =$ 61 mol/(mol h), similar to the values for the three catalysts shown in Table 3. Turnover rates for DBT HDS over Ni_2P/SiO_2 catalysts were 0.0015 [26] and 0.0030 s^{-1} [37], respectively, similar to the corresponding value of the SBA_S catalyst (0.0031 s^{-1} or 11 mol/(mol h)) but much smaller than those of excess phosphorus-containing catalysts (Table 4). Accordingly, the intrinsic hydrotreating activities (or turnover frequencies) of SBA-15-supported catalysts were similar to or even much higher than those of Ni_2P/SiO_2 catalysts published in the literature.

4.5. HDS and HDN reaction pathways

The HDS reaction of DBT proceeds through two different pathways; a hydrogenation (HYD) route and a direct desulfurization (DDS) route. BP and CHB are the main products of the DDS and HYD routes, respectively [39]. Nitrogen-containing molecules are strong inhibitors for the HYD pathway; therefore, in the presence of these molecules, the amount of biphenyl is six to nine times higher than the sum of tetrahydrodibenzothiophene and cyclohexylbenzene [40]. This explains why our BP selectivities were close to 95% over all nickel phosphide catalysts (Fig. 10). Because HDS is a structure-insensitive reaction [12], the biphenyl selectivities are quite stable.

HDN has been suggested to be a structure-sensitive reaction [12]; therefore, the toluene (HDN) selectivities vary greatly over the nickel phosphide catalysts (Fig. 11). The structure sensitivity of HDN arises from structural differences in the active surface phase [12]. Due to the wide variety of HDN conversions (Fig. 11) and toluene selectivities (Fig. 13), the active surface phases are different and changing during the reaction. Because MCH is the final product of both pathways in the HDN reaction network of OMA [11], we cannot differentiate between the preferred reaction routes.

Similar to the HDS reaction of DBT, presumably the HYD route is also suppressed in the HDN reaction of OMA, because, in contrast to silica-supported metal phosphide catalysts [11], the toluene selectivity is always >50% (Fig. 13). Therefore, we agree with [40] that C–N and C–S bond-breaking occur at different active sites, whereas the hydrogenation sites for nitrogen- and sulfur-containing molecules may be the same. The HYD route is more suppressed in both (HDS and HDN) reactions on

the SBA-15 than on the traditional silica-supported nickel phosphide catalysts.

5. Conclusion

We prepared three different $Ni_{12}P_5$- and Ni_2P-containing catalysts supported on ordered SBA-15 mesoporous silica by reduction starting from impregnated nickel phosphate precursors with initial P/Ni molar ratios of 0.5, 0.8, and 2. This varied phosphorus content produced a significant effect on both the structure and activity of the catalysts. Using a stoichiometric phosphorus amount, we obtained $Ni_{12}P_5$ with a relatively homogeneous particle size distribution. For this SBA_S catalyst, active site densities, derived from CO chemisorption and from the nickel phosphide particle size, were in good agreement. On the other hand, when a high excess of phosphorus was used in the preparation (SBA_H) so as to arrive at Ni_2P active phases, CO chemisorption was impeded. Further characterization indicated that the lower accessibility of the Ni_2P particles was caused by pore blocking with phosphate species. A slight excess of phosphorus (SBA_E) also blocked the pores and yielded a mixture of Ni_2P and $Ni_{12}P_5$ in the SBA-15 catalyst. Thus, in the absence of excess phosphate species that block the mesopores, high dispersion of $Ni_{12}P_5$ was observed in SBA-15. The presence of phosphate species resulted in lower CO chemisorption because part of the active phase was not formed (due to partial reduction or reoxidation after passivation), another part was not accessible (due to pore-plugging), and only a small part of nickel was in an accessible Ni_2P form. Whereas the activity per unit catalyst mass was highest in the $Ni_{12}P_5$-containing catalyst, the intrinsic activities per unit accessible sites show that Ni_2P was more active. The SBA-15-supported $Ni_{12}P_5$ catalysts indicated similar activity (turnover rate) to Ni_2P/SiO_2 whilst the SBA-15-supported Ni_2P phase outperformed Ni_2P/SiO_2. Indeed, for ordered mesoporous silica-supported Ni_2P, the excess of phosphate species limited metal utilization in hydrotreating reactions.

Acknowledgments

The authors thank Dr. I. Sajó for providing the XRD patterns, Dr. M. Hegedus for the providing CO adsorption data from the Chemical Research Center (Hungary), Professor J.W. Niemantsverdriet (Eindhoven University of Technology) for providing the XPS measurements, Adelheid Elemans-Mehring and Tiny Verhoeven (Eindhoven University) for providing the ICP-OES and XPS measurements, and Dr. K. Polyak (Pannon University) for determining the elemental composition of the samples. The authors are indebted to Professor J.B. Nagy (FUNDP, Namur, Belgium) for the use of the NMR and TEM facilities. Financial support was provided by the FNRS (Belgium), the GACR (Czech Republic; grant 104/06/0870), the National Creative Research Initiative Program, and the Brain Korea 21 Program.

References

[1] S.T. Oyama, J. Catal. 216 (2003) 343.
[2] R. Iwamoto, J. Grimblot, Adv. Catal. 44 (2000) 417.
[3] R. Prins, V.H.J. de Beer, G.A. Somorjai, Catal. Rev.-Sci. Eng. 31 (1989) 1.
[4] S. Eijsbouts, Ph.D. thesis, Eindhoven University of Technology, Eindhoven, 1989.
[5] W.R.A.M. Robinson, T.I. Korányi, A.M. van der Kraan, V.H.J. de Beer, Final Report, E.C. Contract JOUF-0049-C, 1994.
[6] T.I. Korányi, Appl. Catal. A 239 (2003) 253.
[7] W.R.A.M. Robinson, J.N.M. van Gestel, T.I. Korányi, S. Eijsbouts, A.M. van der Kraan, J.A.R. van Veen, V.H.J. de Beer, J. Catal. 161 (1996) 539.
[8] C. Stinner, R. Prins, Th. Weber, J. Catal. 202 (2001) 187.
[9] V. Zuzaniuk, C. Stinner, R. Prins, Th. Weber, Stud. Surf. Sci. Catal. 143 (2002) 247.
[10] C. Stinner, Z. Tang, M. Haouas, Th. Weber, R. Prins, J. Catal. 208 (2002) 456.
[11] V. Zuzaniuk, R. Prins, J. Catal. 219 (2003) 85.
[12] S.T. Oyama, X. Wang, Y.-K. Lee, W.-J. Chun, J. Catal. 221 (2004) 263.
[13] S.J. Sawhill, D.C. Phillips, M.E. Bussell, J. Catal. 215 (2003) 208.
[14] S.T. Oyama, X. Wang, Y.-K. Lee, K. Bando, F. Requejo, J. Catal. 210 (2002) 207.
[15] S.J. Sawhill, K.A. Layman, D.R. van Wyk, M.H. Engelhard, C. Wang, M.E. Bussell, J. Catal. 231 (2005) 300.
[16] P. Clark, S.T. Oyama, J. Catal. 218 (2003) 78.
[17] Y. Shu, S.T. Oyama, Carbon 43 (2005) 1517.
[18] Y. Shu, S.T. Oyama, Chem. Commun. (2005) 1143.
[19] A. Wang, L. Ruan, Y. Teng, X. Li, M. Lu, J. Ren, Y. Wang, Y. Hu, J. Catal. 229 (2005) 314.
[20] Y.-K. Lee, Y. Shu, S.T. Oyama, Appl. Catal. A 322 (2007) 191.
[21] R. Nava, J. Morales, G. Alonso, C. Ornelas, B. Pawelec, J.L.G. Fierro, Appl. Catal. A 321 (2007) 58.
[22] M. Choi, W. Heo, F. Kleitz, R. Ryoo, Chem. Commun. (2003) 1340.
[23] T.I. Korányi, Z. Vít, J.B. Nagy, Catal. Today 130 (2008) 80.
[24] Z. Vít, J. Cinibulk, D. Gulková, Appl. Catal. A 272 (2004) 99.
[25] Z. Vít, M. Zdražil, J. Catal. 119 (1989) 1.
[26] X. Wang, P. Clark, S.T. Oyama, J. Catal. 208 (2002) 321.
[27] X. Liu, J. Chen, J. Zhang, Catal. Commun. 8 (2007) 1905.
[28] A. Tuel, L. Canesson, J.C. Volta, Colloids Surf. A 158 (1999) 97.
[29] K. Eichele, R.E. Wasylishen, J. Phys. Chem. 98 (1994) 3108.
[30] G.C. Gunter, R. Craciun, M.S. Tam, J.E. Jackson, D.J. Miller, J. Catal. 164 (1996) 207.
[31] T.R. Krawietz, P. Lin, K.E. Lotterhos, P.D. Torres, D.H. Barich, A. Clearfield, J.F. Haw, J. Am. Chem. Soc. 120 (1998) 8502.
[32] A.H. Janssen, P. van der Voort, A.J. Koster, K.P. de Jong, Chem. Commun. (2002) 1632.
[33] S. Yang, C. Liang, R. Prins, J. Catal. 237 (2006) 118.
[34] D. Briggs, M.P. Seah (Eds.), Practical Surface Analysis by Auger and X-Ray Photoelectron Spectroscopy, Wiley, New York, 1983.
[35] J.A. Rodriguez, J.-Y. Kim, J.C. Hanson, S.J. Sawhill, M.E. Bussell, J. Phys. Chem. B 107 (2003) 6276.
[36] A.E. Nelson, M. Sun, A.S.M. Junaid, J. Catal. 241 (2006) 180.
[37] F. Sun, W. Wu, Z. Wu, J. Guo, Z. Wei, Y. Yang, Z. Jiang, F. Tian, C. Li, J. Catal. 228 (2004) 298.
[38] A. Wang, L. Ruan, Y. Teng, X. Li, M. Lu, J. Ren, Y. Wang, Y. Hu, J. Catal. 229 (2005) 314.
[39] M. Houalla, N.K. Nag, A.V. Sapre, D.H. Broderick, B.C. Gates, AIChE J. 24 (1978) 1015.
[40] M. Egorova, R. Prins, J. Catal. 221 (2004) 11.